

# Nonreciprocal Thermal Emission Using Spatiotemporal Modulation of Graphene

Alok Ghanekar,\* Jiahui Wang, Cheng Guo, Shanhui Fan, and Michelle L. Povinelli



Cite This: *ACS Photonics* 2023, 10, 170–178



Read Online

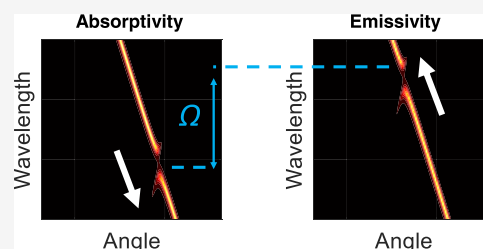
ACCESS |

Metrics & More

Article Recommendations

**ABSTRACT:** We present a nonreciprocal thermal emitter based on the dynamic modulation of graphene. A graphene ribbon grating situated on a dielectric slab is designed to excite high-quality resonances in the long-IR region. We show that upon space–time modulation of the Fermi energy of graphene, asymmetric modal splitting results in large nonreciprocity, leading to a strong violation of Kirchhoff's law of thermal radiation. We further show that the graphene system allows the creation of “absorptivity holes” and “emissivity holes” in the spectrum that are asymmetric. By changing the modulation frequency, the location of these holes can be adjusted, giving rise to a new dimension of tunable thermal emission in nonreciprocal systems. In this system, while Kirchhoff's law is violated, we numerically observe certain symmetry properties between absorption and emission. We establish that these symmetry properties follow compound symmetry considerations.

**KEYWORDS:** *graphene, nonreciprocal emissivity, thermal radiation, dynamic modulation, coupled-mode theory*



## INTRODUCTION

Thermal radiation is a fundamental mode of energy transfer. Control of thermal radiation would allow us to access virtually all sources of energy.<sup>1</sup> A defining aspect of naturally occurring thermal emission is that it is incoherent, diffusive, and broadband.<sup>2,3</sup> Research on sub-wavelength microstructures has demonstrated that the nature of thermal radiation can be fundamentally altered in such materials. For example, previous work has demonstrated the design of narrowband,<sup>4,5</sup> specular,<sup>6,7</sup> and dynamic<sup>8,9</sup> control of thermal radiation. Radiative heat transfer is typically bound by reciprocity, resulting in Kirchhoff's law of thermal radiation. This law states that the emissivity and absorptivity at a given frequency, polarization, and angle of incidence must be equal. Although Kirchhoff's law imposes a fundamental constraint on naturally occurring thermal radiation, it does not originate from the second law of thermodynamics. It is based on Lorentz reciprocity. Therefore, it is possible to violate Kirchhoff's law by breaking reciprocity. Nonreciprocity may enable achieving the ultimate efficiency limits for solar energy harvesting, namely, the Landsberg limit.<sup>10,11</sup>

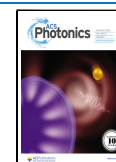
So far, the majority of work on violation of Kirchhoff's law is focused on magneto-optical materials.<sup>12–14</sup> Our previous work demonstrated a novel, alternative approach to attaining nonreciprocal thermal emission using traveling wave index modulation.<sup>15</sup> This route provides a promising direction for developing nonreciprocal thermal emitters without using magneto-optics. A limitation of space–time-modulated thermal emitters is that the wavelength range for nonreciprocal thermal emission is limited by choice of electro-optic material. In this case, changing the operating wavelength may require changing

the entire material system. Besides, strong modulation of the refractive index is difficult to realize for traditional electro-optic materials. Here, we take advantage of the tunability of graphene to show that highly tunable absorption and emission of thermal radiation are possible. Graphene represents a very promising medium for the exploration of the consequence of dynamic modulation on thermal radiation. Along with a wide tunability in the infrared regime,<sup>16,17</sup> graphene has demonstrated the capability of high-speed, all-optical modulation at large modulation depths.<sup>18</sup> This allows the exploration of exciting new possibilities for tunable nonreciprocal emission.

In this work, we design a nonreciprocal thermal emitter based on dynamic modulation of the optical conductivity of graphene. We use graphene to modulate the guided modes of a dielectric layer, producing tunable modes with high-quality factors >5000. Utilizing the formulation developed in our previous work, we calculate absorptivity and emissivity numerically. We show that dynamic modulation of the Fermi level of graphene enables violation of Kirchhoff's law in the long-IR region. Moreover, by varying the emitter geometry, strong contrast between emissivity and absorptivity can be obtained over a broad range of wavelengths and incident angles. Our numerical results show that while the system does not observe the Kirchhoff law, there is

**Received:** September 8, 2022

**Published:** December 30, 2022



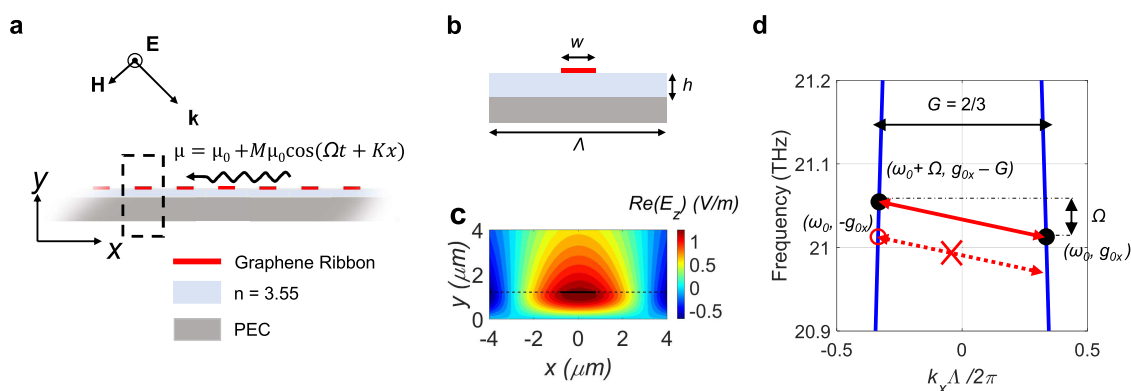


**Figure 1.** (a) Graphene-based grating design. Graphene ribbons situated over a dielectric slab undergo dynamic, traveling wave modulation of Fermi energy. The dashed lines indicate one unit cell of the grating. (b) Detail of unit cell with period  $\Lambda$ , slab height  $h$ , and ribbon width  $w$ . (c) Modal profile of a guided mode excited by an oblique angle of incidence around normalized wave vector  $g_{0x} \equiv k_{0x}\Lambda/2\pi = 1/3$ . The modal profile extends through the graphene layer, allowing tunability and modulation of guided modes. (d) Calculated band structure of the grating with  $\Lambda = 8 \mu\text{m}$ ,  $h = 1.2 \mu\text{m}$ , and  $w = 1.6 \mu\text{m}$ , highlighting resonant modes of interest. Modes located at  $(\omega_0, g_{0x})$  and  $(\omega_0 + \Omega, g_{0x} - G)$  can be coupled by the dynamic modulation with temporal frequency  $\Omega$  and spatial frequency  $G = K\Lambda/2\pi = 2/3$ . The mode located at  $(\omega_0, -g_{0x})$  cannot couple with any mode on the band on the right side due to phase mismatch.

a symmetry relation between absorptivity and emissivity. In particular, the absorptivity at a given angle and wavelength is equal to the emissivity at the opposite angle. We explore the origin of this result within coupled-mode theory and then establish that it follows from general compound symmetry arguments. The result is useful for computation, allowing one to compute emissivity by absorption calculations. Moreover, we propose that modulation of graphene allows the possibilities of creating absorptivity and emissivity “holes,” angle-wavelength pairs for which absorptivity or emissivity are suppressed due to dynamic modulation. This suggests intriguing new possibilities for tunable modulation of infrared absorption and emission spectra of materials, motivating experimental implementations.

## RESULTS AND DISCUSSION

We start by briefly reviewing the dynamic-modulation-based mechanism for achieving nonreciprocal thermal radiation, as proposed in ref 15. A refractive index modulation that varies with space and time can break reciprocity. The scattering matrix of such an object is asymmetric, i.e.,  $S \neq S^T$ .

We assume that the modulation frequency is much less than the frequency at which emissivity and absorptivity are calculated. In a space–time-modulated system, when the modulation frequency is far below that of the photons, photon flux is conserved during frequency-conversion processes, as described by the Manley–Rowe relation.<sup>19,20</sup> Therefore, emissivity and absorptivity can be defined in terms of photon flux. With these considerations, formalism developed in ref 21 remains valid for time-modulated systems. We define an absorptivity matrix,  $A$ , and an emissivity matrix that are related to the scattering matrix of the system,  $S$ , by

$$A = I_I - S^\dagger S \quad (1)$$

and

$$E = I_O - SS^\dagger \quad (2)$$

In our previous work, we demonstrated that in the presence of loss, matrices  $A$  and  $E$  could be unequal, violating Kirchhoff's law of thermal radiation. Such a modulation mechanism involves the modulation of the refractive index of the dielectric slab. Here, we show that an array of graphene ribbons can be employed to

create and modulate guided modes in a dielectric slab, eliminating the need for electro-optic modulation of the dielectric.

**Nonreciprocal Emission with Graphene.** We begin by analyzing a guided-mode resonance grating with graphene. We show that space–time modulation of the Fermi energy of graphene can be utilized to create nonreciprocity. Figure 1a shows the graphene-based grating structure considered in the present study. A grating consisting of a periodic array of monolayer graphene ribbons is situated over a dielectric slab. The refractive index of the dielectric is taken to be 3.55, and the bottom layer is assumed to be a perfect electrical conductor. The unit cell of the grating is shown in Figure 1b. The period of the grating is  $\Lambda$ ; the dielectric slab has a height of  $h$ , and the graphene ribbons have a width of  $w$ .

The dimensions of the grating are chosen to support guided resonances in the longwave-IR region. We consider the transverse electric (TE) polarization, where only the  $z$ -component of the electric field is nonzero. Previous work has used the plasmonic resonances of graphene for tunable thermal emission/absorption.<sup>17</sup> However, plasmonic resonances are typically lossy, resulting in low-quality factors. High-quality guided modes can also be created and tuned using graphene-based structures using TE polarization.<sup>22</sup> This polarization does not excite plasmons in the graphene layer; the presence of the graphene grating instead enables the excitation of guided modes in the dielectric layer. The field profile of a guided mode in our grating structure is shown in Figure 1c. We calculated the associated quality factor to be  $\sim 5500$ . The modal field extends through the graphene layer, allowing for modulation.

We assume that the Fermi level of graphene undergoes a spatiotemporal modulation represented by  $\mu = \mu_0 + M\mu_0 \cos(\Omega t + Kx)$ . Here,  $\mu_0$  is the base Fermi level of graphene,  $M$  is the amplitude of modulation (modulation strength),  $\Omega$  is the modulation frequency, and  $K$  is the spatial frequency of modulation. Such dynamic modulation can couple any modes that are separated by the modulation vector, i.e., by both the modulation frequency and the spatial frequency of modulation. We calculate the band structure of the unmodulated grating with  $\Lambda = 8 \mu\text{m}$ ,  $h = 1.2 \mu\text{m}$ , and  $w = 1.6 \mu\text{m}$  and plot the results in Figure 1d. The parallel wave vector is shown in normalized units  $g_x = k_x\Lambda/2\pi$ , while the frequency is shown in real units of THz.

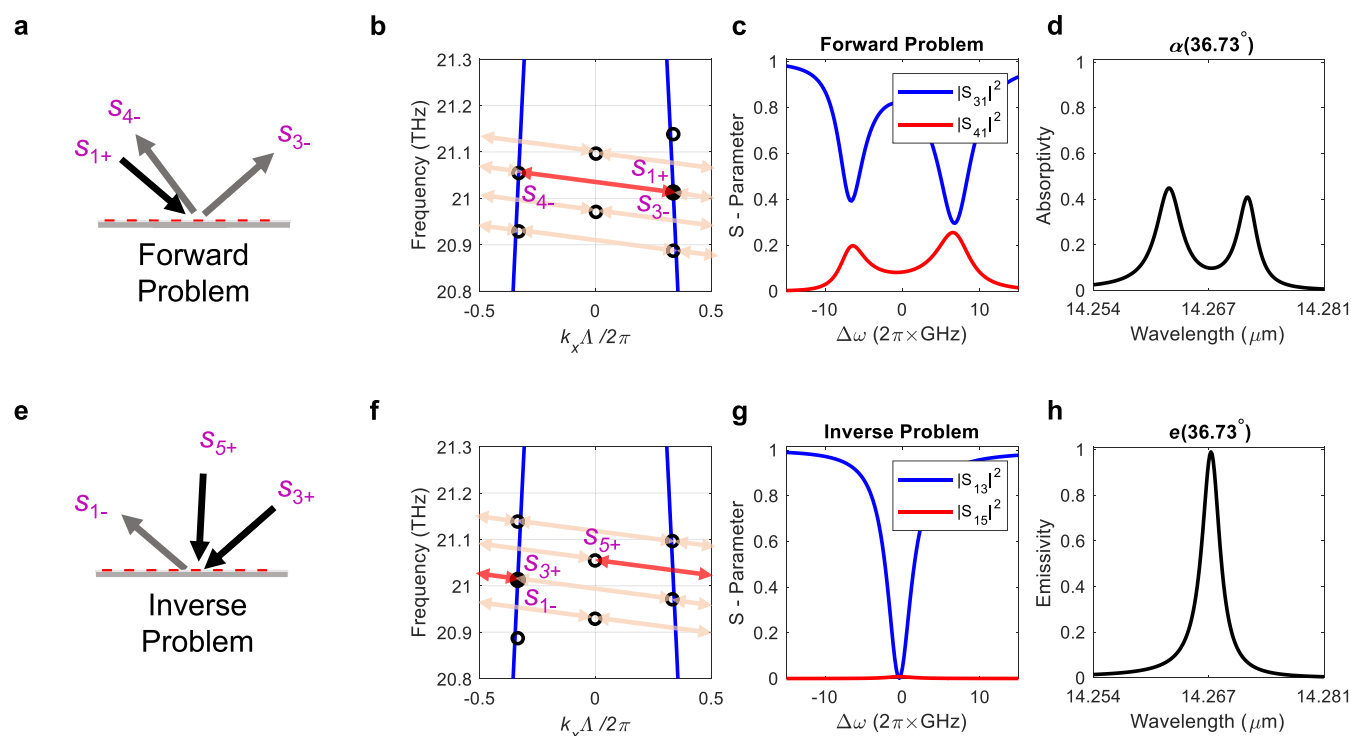


**Figure 2.** Strongly modulated system with  $M = 0.2$ . (a) Forward problem with incoming wave  $s_{1+}$  and outgoing waves  $s_{3-}$  and  $s_{4-}$ . (b) Incoming wave from  $s_{1+}$  can couple to modes separated by the modulation vector. (c) S-parameters calculated for the forward problem at port 1. (d) Calculated absorptivity at port 1. (e) Inverse problem with an outgoing wave  $s_{1-}$  given rise by incoming waves at  $s_{3+}$  and  $s_{5+}$ . (f) Modes indicated by black circles ( $\omega_0 + n\Omega, -g_{0x} - nG$ ) that can produce output mode  $s_{1-}$ . Red arrows indicate the coupling with modes that make a non-negligible contribution to  $s_{1-}$ . (g) S-parameters calculated for the inverse problem at port 1. (h) Calculated emissivity at port 1.

Figure 1d also displays resonant modes that are separated by the modulation frequency  $\Omega$ , and the normalized spatial frequency of modulation,  $G \equiv K\Lambda/2\pi$ . Modes located at  $(\omega_0, g_{0x})$  and  $(\omega_0 + \Omega, g_{0x} - G)$  can be coupled due to the modulation (shown by a solid red arrow). However, the mode  $(\omega_0, -g_{0x})$  cannot couple to any mode on the band on the right side (indicated by the dashed arrow). As shown below, this asymmetric coupling forms the basis of nonreciprocal scattering,<sup>23</sup> leading to a violation of Kirchhoff's law of thermal radiation.<sup>15</sup>

To numerically model the graphene-based dynamic system, we must modify the approach of ref 24 to include the optical conductivity of graphene. The optical conductivity ( $\sigma$ ) of graphene can be modeled as a Drude response in the infrared region,<sup>25</sup> and it is directly proportional to the chemical potential

$$\sigma = \frac{e^2 \mu}{\pi \hbar^2} \frac{\tau}{(1 - i\omega\tau)} \quad (3)$$

Here,  $e$  is the elementary charge,  $\hbar$  is the reduced Planck's constant,  $\omega$  is the angular frequency, and  $\tau$  is the relaxation time. In our simulation, we assume that the base Fermi energy of graphene ( $\mu_0$ ) is 0.5 eV. The relaxation time  $\tau$  is taken to be 0.5 ps. For  $\Omega \ll \omega$ , we neglect dispersion in eq 3 and approximate  $\sigma$  by its value at  $\omega_0$ . A spatiotemporal modulation of graphene thus implies a sinusoidal dependence of optical conductivity  $\sigma(x, t) = \sigma_0 + M\sigma_0 \cos(\Omega t + Kx)$ , where  $\sigma_0 = \sigma(\omega_0)$  from eq 3. We then take the conductivity to be constant within each ribbon, such that  $\sigma = \sigma_0 + M\sigma_0 \cos(\Omega t + \phi)$ , where the phase difference between adjacent ribbons  $\Delta\phi = K\Lambda$ .

Using Ohm's law  $J(t) = \sigma(t)E(t)$ , we obtain

$$J(t) = \left( \sigma_0 + \frac{M\sigma_0}{2} e^{+i(\Omega t + \phi)} + \frac{M\sigma_0}{2} e^{-i(\Omega t + \phi)} \right) E(t) \quad (4)$$

Fourier-transforming eq 4, we can show that the current density in graphene is coupled across different frequencies, as given by the equation

$$J(\omega_n) = \sigma_0 E_n + \frac{M\sigma_0}{2} e^{+i\phi} E_{n-1} + \frac{M\sigma_0}{2} e^{-i\phi} E_{n+1} \quad (5)$$

Here,  $J(\omega_n)$  is the current density term for graphene in the  $n$ th harmonic  $\omega_n = \omega_0 + n\Omega$ , and  $E_n$  is the electric field.

The simulation proceeds by calculating the fields at the excitation frequency  $\omega_0$  and at sideband frequencies  $\omega_0 \pm \Omega$ ,  $\omega_0 \pm 2\Omega$ , and  $\omega_0 \pm 3\Omega$  in COMSOL. Each time-harmonic field is represented by a separate physics node in the simulation. In our analysis,  $G$  is taken to be  $2/3$ . This leads to  $\Delta\phi = 4\pi/3$ . We considered 3-unit periods to simulate the modulated grating and imposed Floquet periodic boundary conditions for all time harmonics. The phase difference between the boundaries is a multiple of  $2\pi$ . The simulation method allows us to calculate the S-parameters of the system.

The absorptivity and emissivity of the space–time-modulated system can be obtained from the S-parameters using the formalism of ref 21. In a space–time-modulated system, photon flux is conserved during the frequency-conversion process.<sup>20,26</sup> Therefore, the absorptivity and emissivity must be defined in terms of photon flux rather than power.<sup>15</sup> To calculate the absorptivity of a given port, we first consider the forward problem, shown in Figure 2a. The absorptivity of port 1 is given by

$$\alpha_1 = 1 - \sum_q |S_{q1}|^2 \quad (6)$$

where  $S_{q1}$  is the S-matrix element defined as  $s_{q-}/s_{1+}$ . Here, the sum is taken over all possible output amplitudes  $q$  generated by the input  $s_{1+}$ .

Consider an incident wave  $s_{1+}$  in free space, as shown schematically in Figure 2a. To couple to the grating mode indicated by the solid black dot of Figure 2b, the incoming wave should have the same wave vector and frequency as the grating mode. We therefore choose the incident wave vector to be  $g_{0x} = +1/3 + \Delta$ . We choose  $\Delta = 0.002$ , corresponding to an incident angle of  $\sin^{-1}(\omega_0/k_{0x}) = 36.73^\circ$  and angular frequency  $\omega_0 = 2\pi \times 21.014$  THz. Since the period of the grating is smaller than the wavelength ( $14.3 \mu\text{m}$ ), diffraction into higher orders does not occur. In the absence of modulation, a part of the incident wave is absorbed, and the rest is reflected, exiting into port 3 with amplitude  $s_{3-}$ .

We now introduce a modulation to create a nonzero output into  $s_{4-}$ . We consider a spatial frequency  $G = 2/3$ , for which the modulation repeats every three periods of the grating. We choose the modulation frequency to couple the mode at  $g_{0x} = +1/3 + \Delta$  to the mode at  $g_{0x} - G = -1/3 + \Delta$ , giving a value of  $\Omega = 2\pi \times 41.89$  GHz. The coupling is indicated schematically by the red arrow on the band structure of Figure 2b. We note that a finite, nonzero value of  $\Delta$  is required in our nonreciprocity scheme to correspond to a nonzero modulation frequency.

For sufficiently strong modulation, higher harmonics can, in principle, also be excited at  $\omega_0 + n\Omega$  and  $g_{0x} - nG$ . The higher harmonics are denoted by hollow black circles in Figure 2b. All of these output modes are plane waves that propagate in free space with different angles given by  $\theta = \sin^{-1}(\omega_n/k_{nx})$ . In our numerical simulations, we calculate the corresponding scattering matrix elements. We refer to any scattering matrix elements for which  $|S_{q1}|^2 > 1 \times 10^{-3}$  as "significant" and neglect the rest.

Figure 2c shows the numerical results of the scattering matrix calculation for a system with  $M = 0.2$ . We plot  $|S_{31}|^2$  and  $|S_{41}|^2$  in Figure 2c, the only significant elements. Higher harmonics were not significant. From Figure 2c, we see that the spectrum is asymmetric around the central frequency and exhibits mode splitting. It is known as Rabi splitting, which occurs due to strong coupling between the modes. The resulting absorptivity spectrum also shows modal splitting (Figure 2d).

To calculate the emissivity of port 1, we consider the inverse problem, as shown in Figure 2e. The emissivity of port 1 is given by<sup>15,21</sup>

$$e_1 = 1 - \sum_q |S_{1q}|^2 \quad (7)$$

Here, the sum is taken over all possible input amplitudes  $q$  can produce for the output  $s_{1-}$ . Therefore, emissivity calculations at port 1 involve identifying all inputs ( $\omega_0 + n\Omega$ ,  $-g_{0x} - nG$ ) that can give rise to output  $s_{1-}$  ( $\omega_0$ ,  $-g_{0x}$ ). The corresponding modes are shown by hollow circles in Figure 2f. The largest scattering matrix element arises from specular reflection ( $|S_{13}|^2$ ). The only other significant scattering matrix element was found to be  $|S_{15}|^2$ . This matrix element involves coupling from an input that is not  $(k, \omega)$  matched to any grating mode and increases in value with the modulation strength. The values of the significant scattering matrix elements are plotted in Figure 2g. The contribution of  $|S_{15}|^2$  is small, and the emissivity of port 1 is similar to the unmodulated system. The emissivity does not exhibit modal splitting (Figure 2h). Comparing Figure 2d,h, a strong contrast

between emissivity and absorptivity is seen, indicating a violation of Kirchhoff's Law.

The ability to tune the optical conductivity of graphene over a broad bandwidth in the longwave infrared allows strong flexibility in design. By choosing the appropriate grating geometry, we can tune both the angle and wavelength of nonreciprocal thermal emission. For illustration, we consider three different grating designs, as shown in Table 1. Design A is

**Table 1. Different Geometrical Parameters for Designs A, B, and C.  $\lambda$  and  $\theta$  are the Approximate Wavelengths and Angles at Which Nonreciprocal Thermal Emission is Obtained**

design	$\Lambda$ ( $\mu\text{m}$ )	$w$ ( $\mu\text{m}$ )	$h$ ( $\mu\text{m}$ )	$\lambda$ ( $\mu\text{m}$ )	$\theta$ ( $^\circ$ )
A	8	1.6	1.2	14.26	36.73
B	8	1.6	1.1	13.47	34.38
C	5	1.6	1.2	12.13	54.47

the geometry studied above ( $\Lambda = 8 \mu\text{m}$ ,  $h = 1.2 \mu\text{m}$ , and  $w = 1.6 \mu\text{m}$ ). Designs B and C change the slab height and periodicity, respectively. We choose a modulation frequency  $\Omega$  of 41.89 GHz, spatial frequency  $G = 2/3$ , and modulation strength  $M = 0.2$ , as before.

To examine the effect of slab height  $h$ , we plot the band structure of design A ( $h = 1.2 \mu\text{m}$ ) and design B ( $h = 1.1 \mu\text{m}$ ) in Figure 3a. Here, the wave vector is plotted in rad/m. We notice that the Brillouin zone spans from  $-\pi/\Lambda$  to  $+\pi/\Lambda$ . With a change in the slab height, the band structure shifts. The resonances that couple via the modulation vector are different for the two designs (indicated by open, black circles) and occur

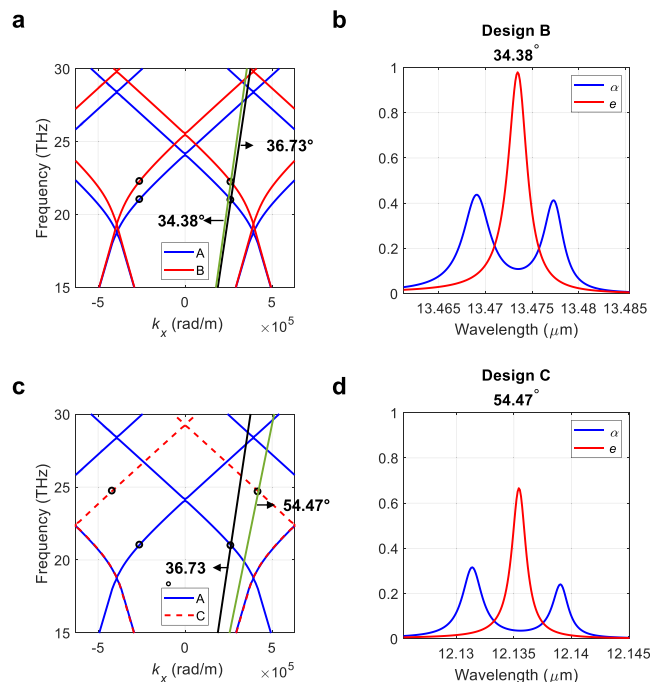


**Figure 3.** (a) Effect of slab height: band diagrams of the grating design A and grating design B ( $\Lambda = 8 \mu\text{m}$ ,  $h = 1.1 \mu\text{m}$ , and  $w = 1.6 \mu\text{m}$ ) plotted with wave vector in SI units. (b) Calculated absorptivity and emissivity for design B around  $13.47 \mu\text{m}$  at an angle of incidence of  $34.38^\circ$ . (c) Effect of periodicity: band diagrams of the grating design A and grating design C ( $\Lambda = 5 \mu\text{m}$ ,  $h = 1.2 \mu\text{m}$ , and  $w = 1.6 \mu\text{m}$ ) plotted with wave vector in SI units. (d) Calculated absorptivity and emissivity for design C around  $12.13 \mu\text{m}$  at an angle of incidence of  $54.47^\circ$ .



at different wave vectors and frequencies. As a result, nonreciprocal thermal emission manifests at a different wavelength and angle of incidence. The  $\theta = \text{constant}$  lines are plotted in Figure 3a. While design A exhibits nonreciprocal thermal emission at  $36.73^\circ$ , design B exhibits nonreciprocal thermal emission at a smaller angle of  $34.38^\circ$ . Figure 3b plots the absorptivity and emissivity for design B. The emissivity peaks at approximately  $13.47 \mu\text{m}$  shifted down in wavelength (up in frequency) concerning design A (approximately  $14.27 \mu\text{m}$ ).

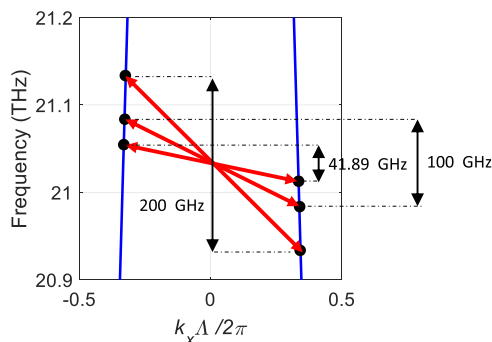


**Figure 4.** Effect of varying the modulation frequency on modal coupling. The red arrows indicate three sample modulation vectors; each has the same horizontal length (spatial wave vector) and different vertical heights (modulation frequency). As the modulation frequency is varied, different modes of the band structure are coupled.

Figure 3c shows the effect of the periodicity of the grating on the band diagram. The modes of gratings A and C overlap. Because grating C has a smaller periodicity and hence a larger Brillouin zone, the bands of grating C (red, dashed lines) fold at a larger  $k_x$  than grating A. Consequently, we observe that the

resonances coupled by the modulation vector (open, black circles) occur at noticeably different wave vectors (angle) and wavelength. Constant angle lines are plotted in Figure 3c. The absorptivity and emissivity for design C are shown in Figure 3d. A strong contrast between absorptivity and emissivity is observed around  $12.135 \mu\text{m}$  for an angle of incidence of  $54.47^\circ$ .

The results of changing grating geometry are summarized in Table 1. For the three designs presented, the nonreciprocal angle is tuned from approximately  $34$ – $54^\circ$ , while the nonreciprocal wavelength is from approximately  $12$ – $14 \mu\text{m}$ . Further tuning can be achieved with larger variations of period or slab height.

**Tuning the Nonreciprocal Behavior.** By varying the modulation frequency, we can tune the angle and wavelength at which nonreciprocity occurs. For the modulation scheme described above, the spatial modulation frequency is fixed at  $G = 2/3$ . This corresponds to a fixed horizontal length of the modulation vector. As the modulation frequency  $\Omega$  is varied, the vertical height of the modulation vector changes. This is illustrated in Figure 4. As can be seen from the figure, each choice of modulation frequency (e.g., 41.89, 100, or 200 GHz) couples different pairs of modes in the band structure. In general, for two linear bands with opposite slopes, and for any modulation frequency  $\Omega$ , there exists a  $\omega_0$  and  $\Delta$  such that modes  $(\omega_0, 1/3 + \Delta)$  and  $(\omega_0, -1/3 + \Delta)$  can couple, while the mode at  $(\omega_0, -1/3 - \Delta)$  cannot couple to any modes. Nonreciprocity can thus be attained as long as the modulation frequency is larger than the linewidth of the resonances.<sup>23</sup>

We plot absorptivity and emissivity as a function of wavelength and angle of incidence for  $M = 0.2$ ,  $G = 2/3$ , and  $\Omega = 41.89 \text{ GHz}$  in Figure 5a. For negative angles of incidence (leftmost graph), the absorptivity plot shows a single, bright band. This band arises from resonant absorptive enhancement at the guided resonance of the unmodulated grating.<sup>27</sup> Because the

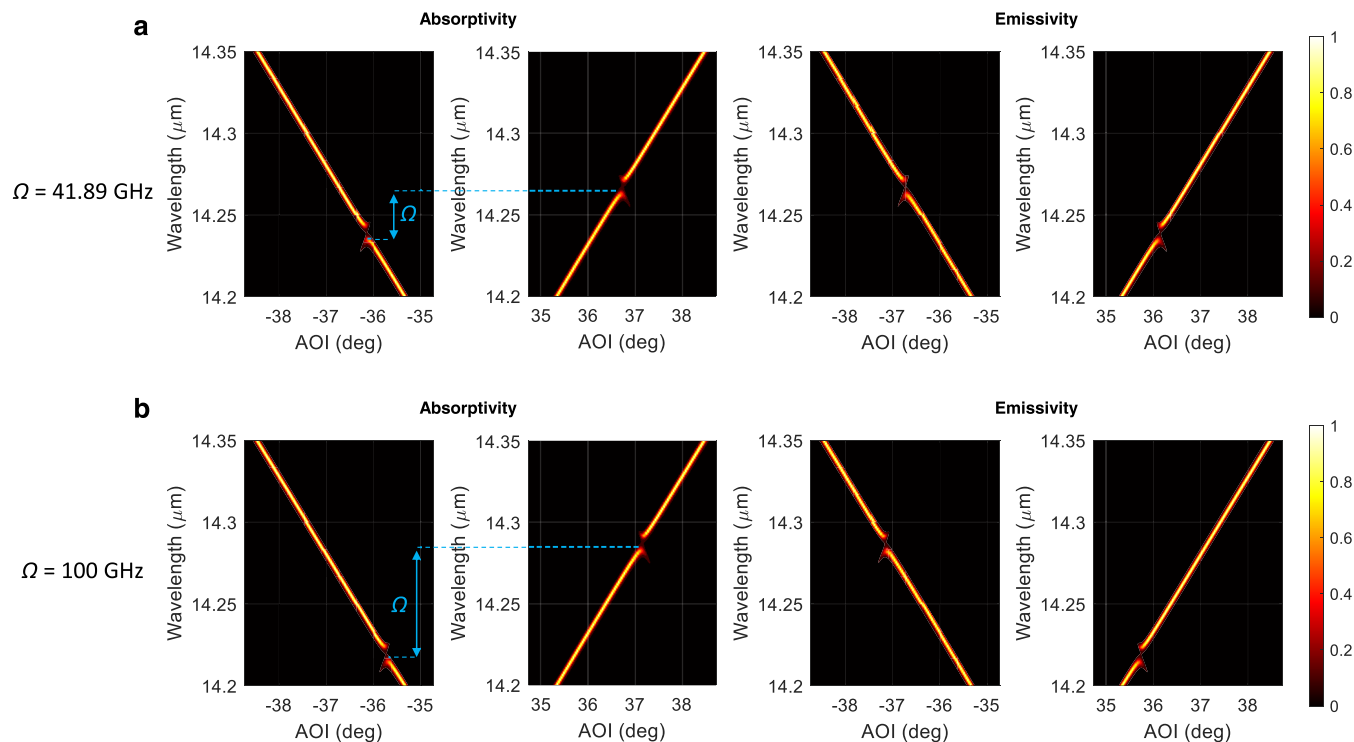


**Figure 5.** Absorptivity and emissivity of a strongly modulated system with  $M = 0.2$  plotted against the wavelength and angle of incidence for (a)  $\Omega = 41.89 \text{ GHz}$  and (b)  $\Omega = 100 \text{ GHz}$ .

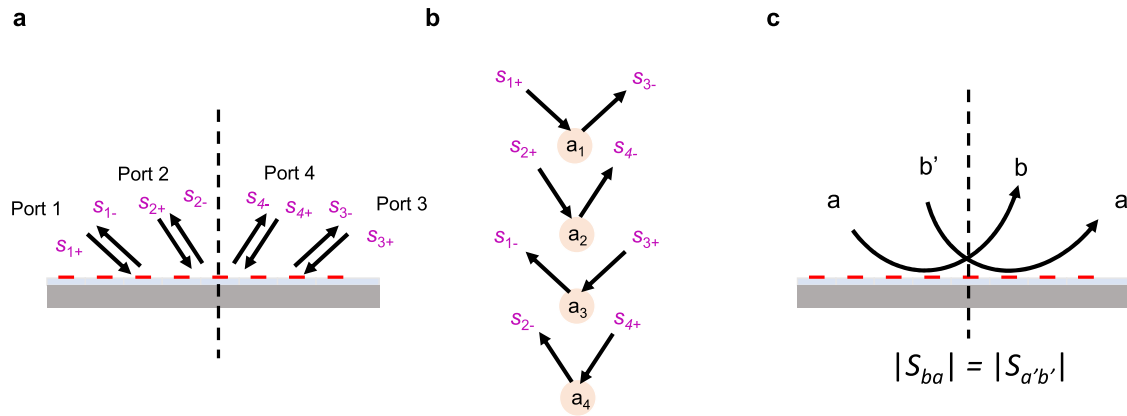


**Figure 6.** (a) Setup displaying a four-port system considered for the coupled-mode theory formulation. Port 1 (port 2) and port 3 (port 4) are mirror partners. They have the same frequency but opposite parallel wave vectors. (b) Naming convention for ports and modes. Modes 1, 2, 3, and 4 are excited by incoming waves  $s_{1+}$ ,  $s_{2+}$ ,  $s_{3+}$ , and  $s_{4+}$ , respectively. Modes 1, 2, 3, and 4 outcouple to waves  $s_{3-}$ ,  $s_{4-}$ ,  $s_{1-}$ , and  $s_{2-}$ , respectively, (c) Hermitian coupling matrix enforces pairing between S-parameters, even though S-matrix is non-Hermitian. Here, port  $a$  ( $b$ ) and  $a'$  ( $b'$ ) are mirror partners.

strongly modulated system exhibits Rabi splitting, as shown above in Figure 5a, the bright absorptivity band appears to have a “hole,” or dark spot, close to 36.73 and 14.26  $\mu\text{m}$ . Due to nonreciprocity, the location of this hole is different than for positive angles of incidence (second graph from the left in Figure 5a). The contour plots for emissivity also show the presence of “holes” in the bright band. The locations of these holes are exactly at an opposite angle to a corresponding absorptivity hole. This indicates the presence of a residual symmetry in the system.

By increasing the modulation frequency, the absorptive and emissive holes move within the band structure, as shown in Figure 5b. The negative-angle absorptive hole is shifted down in wavelength (leftmost plot), while the positive-angle absorptive hole is shifted up. This shift can be explained by observing that the wavelength separation between the positive- and negative-angle holes corresponds to the modulation frequency (indicated schematically by the blue dashed lines).

**Symmetry Considerations.** The relationship between emissivity and absorptivity for opposite angles is a known result for certain time-invariant systems. This observation is not immediately obvious in a time-modulated system. We now explore a possible explanation of symmetry in absorption and emission using coupled-mode theory (CMT). We formulate expressions for absorptivity and emissivity for a 4-port system using CMT. Consider the system shown in Figure 6a, which contains the mirror plane indicated by the dashed lines. We assume that port 1 and port 3 are mirror partners, as are ports 2 and 4. Mirror partners have the same frequency and wave vectors that are related by mirror symmetry. As shown in Figure 6b, we assume that input amplitudes  $s_{1+}$ ,  $s_{2+}$ ,  $s_{3+}$ , and  $s_{4+}$  excite modes  $a_1$ ,  $a_2$ ,  $a_3$ , and  $a_4$ , respectively. We further assume that modes  $a_1$ ,  $a_2$ ,  $a_3$ , and  $a_4$  outcouple to ports 3, 4, 1, and 2, with amplitudes  $s_{3-}$ ,  $s_{4-}$ ,  $s_{1-}$ , and  $s_{2-}$ , respectively. We restrict ourselves to the case when there are no diffraction orders present, as the periodicity ( $\Lambda$ ) is smaller than the wavelength of interest. The steady-state interaction between inputs, outputs, and modes can be described as<sup>28</sup>

$$\begin{aligned} s_{3-} &= c_1 s_{1+} + \sqrt{2\gamma_1^{\text{rad}}} a_1 \\ s_{4-} &= c_2 s_{2+} + \sqrt{2\gamma_2^{\text{rad}}} a_2 \\ s_{1-} &= c_3 s_{3+} + \sqrt{2\gamma_3^{\text{rad}}} a_3 \\ s_{2-} &= c_4 s_{4+} + \sqrt{2\gamma_4^{\text{rad}}} a_4 \end{aligned} \quad (8)$$

Here,  $\gamma_n^{\text{rad}}$  is the radiative decay rate of mode  $a_n$ , and  $c_n$  represents the direct scattering between port  $n$  and its mirror partner. The naming convention for the ports and modes is illustrated in Figure 6b.

The evolution of the modal amplitudes  $a_1$  through  $a_4$  is determined by their coupling to the inputs and each other, according to

$$D \begin{bmatrix} a_1 \\ a_2 \\ a_3 \\ a_4 \end{bmatrix} = \begin{bmatrix} \sqrt{2\gamma_1^{\text{rad}}} s_{1+} \\ \sqrt{2\gamma_2^{\text{rad}}} s_{2+} \\ \sqrt{2\gamma_3^{\text{rad}}} s_{3+} \\ \sqrt{2\gamma_4^{\text{rad}}} s_{4+} \end{bmatrix} \quad (9)$$

where  $D$  is the matrix given by

$$D = \begin{bmatrix} (i\Delta\omega + \gamma_1) & -i\kappa_{12} & -i\kappa_{13} & -i\kappa_{14} \\ -i\kappa_{21} & (i\Delta\omega + \gamma_2) & -i\kappa_{23} & -i\kappa_{24} \\ -i\kappa_{31} & -i\kappa_{32} & (i\Delta\omega + \gamma_3) & -i\kappa_{34} \\ -i\kappa_{41} & -i\kappa_{42} & -i\kappa_{43} & (i\Delta\omega + \gamma_4) \end{bmatrix} \quad (10)$$

Here,  $\kappa_{mn}$  denotes the coupling constant between modes  $m$  and  $n$ ,  $\gamma_n = \gamma_n^{\text{loss}} + \gamma_n^{\text{rad}}$  is the total loss rate,  $\gamma_n^{\text{loss}}$  is the intrinsic loss rate, and  $\Delta\omega = \omega - \omega_n$  is the attenuation from the resonance frequency of the mode.

The modal amplitudes can be calculated as

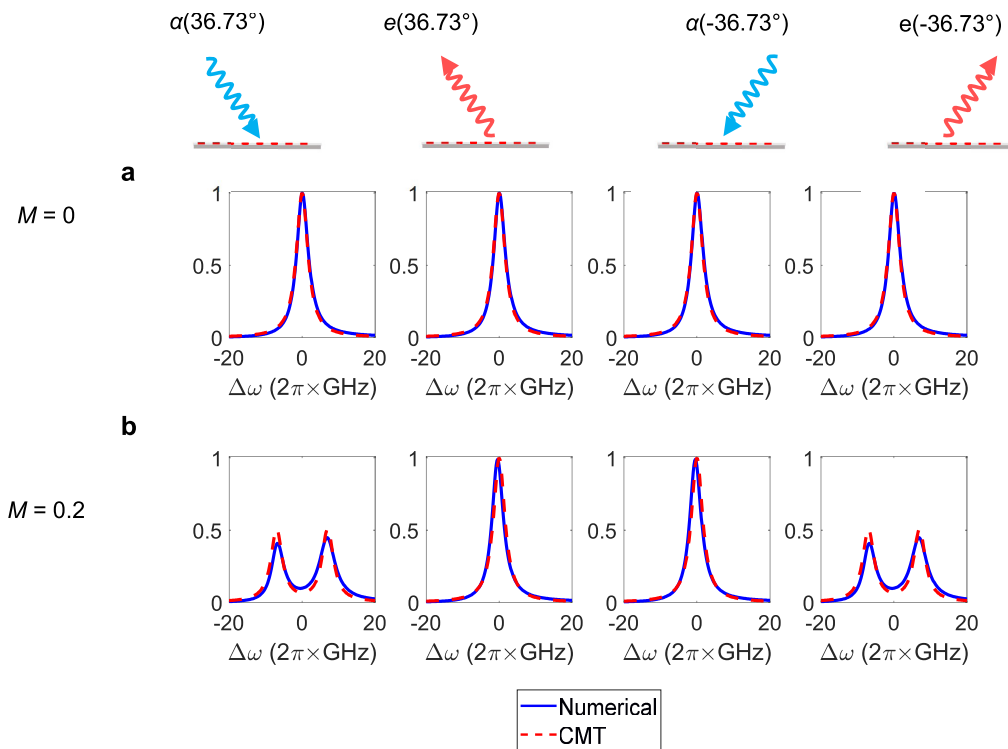


**Figure 7.** Emissivity and absorptivity at port 1 and port 3 for (a) unmodulated system and (b) strongly modulated system with  $M = 0.2$ . Numerical simulations are compared with coupled-mode theory calculations.

$$\begin{bmatrix} a_1 \\ a_2 \\ a_3 \\ a_4 \end{bmatrix} = F \begin{bmatrix} \sqrt{2\gamma_1^{\text{rad}}} s_{1+} \\ \sqrt{2\gamma_2^{\text{rad}}} s_{2+} \\ \sqrt{2\gamma_3^{\text{rad}}} s_{3+} \\ \sqrt{2\gamma_4^{\text{rad}}} s_{4+} \end{bmatrix} \quad (11)$$

where  $F = D^{-1}$ . One can show that if the condition  $\kappa_{mn} = \kappa_{nm}^*$  is satisfied, then  $F_{mn} = F_{nm}^*$ . Using eq 8, the  $S$ -matrix can be calculated as

$$S = \begin{bmatrix} F_{31}\sqrt{4\gamma_1^{\text{rad}}\gamma_3^{\text{rad}}} & F_{32}\sqrt{4\gamma_2^{\text{rad}}\gamma_3^{\text{rad}}} \\ F_{41}\sqrt{4\gamma_1^{\text{rad}}\gamma_4^{\text{rad}}} & F_{42}\sqrt{4\gamma_2^{\text{rad}}\gamma_4^{\text{rad}}} \\ c_1 + F_{11}\sqrt{4\gamma_1^{\text{rad}}\gamma_1^{\text{rad}}} & F_{12}\sqrt{4\gamma_2^{\text{rad}}\gamma_1^{\text{rad}}} \\ F_{21}\sqrt{4\gamma_1^{\text{rad}}\gamma_2^{\text{rad}}} & c_2 + F_{22}\sqrt{4\gamma_2^{\text{rad}}\gamma_2^{\text{rad}}} \\ c_3 + F_{33}\sqrt{4\gamma_3^{\text{rad}}\gamma_3^{\text{rad}}} & F_{34}\sqrt{4\gamma_4^{\text{rad}}\gamma_3^{\text{rad}}} \\ F_{43}\sqrt{4\gamma_3^{\text{rad}}\gamma_4^{\text{rad}}} & c_4 + F_{44}\sqrt{4\gamma_4^{\text{rad}}\gamma_4^{\text{rad}}} \\ F_{13}\sqrt{4\gamma_3^{\text{rad}}\gamma_1^{\text{rad}}} & F_{14}\sqrt{4\gamma_4^{\text{rad}}\gamma_1^{\text{rad}}} \\ F_{23}\sqrt{4\gamma_3^{\text{rad}}\gamma_2^{\text{rad}}} & F_{24}\sqrt{4\gamma_4^{\text{rad}}\gamma_2^{\text{rad}}} \end{bmatrix} \quad (12)$$

where  $S$  is defined by the relation

$$\begin{bmatrix} s_{1-} \\ s_{2-} \\ \vdots \\ s_{n-} \end{bmatrix} = \begin{bmatrix} S_{11} & S_{12} & \cdots & S_{1n} \\ S_{21} & \ddots & & \\ \vdots & & \ddots & \\ S_{n1} & \cdots & \cdots & S_{nn} \end{bmatrix} \begin{bmatrix} s_{1+} \\ s_{2+} \\ \vdots \\ s_{n+} \end{bmatrix} \quad (13)$$

It can be seen by inspection that  $|S_{21}| = |S_{34}|$ ,  $|S_{23}| = |S_{14}|$ , etc.

For simplicity, the equations above are written for a 4-port system. The arguments generalize to a system with  $2N$  ports consisting of  $N$  ports and their  $N$  mirror partners. In general, for any given ports  $a$  and  $b$  and their mirror partners  $a'$  and  $b'$ , respectively,  $|S_{ba}| = |S_{a'b'}|$ . Therefore,  $S$ -parameters in the  $S$ -matrix appear in pairs, even though the  $S$ -matrix is non-Hermitian. This pairing of  $S$ -parameters is schematically shown in Figure 6c. By substituting these equalities in eqs 6 and 7, it can be readily seen that

$$\alpha_a = e_{a'} \quad (14)$$

In other words, the absorptivity of a given port is the same as the emissivity of its mirror partner. That is,

$$\alpha(\omega, k_x) = e(\omega, -k_x) \quad (15)$$

which is what we observe from numerical simulations.

Equation 15 eliminates the need to solve the inverse problem to obtain emissivity, simplifying calculations. The result applies quite generally, provided that higher diffraction orders are not present, as the presence of higher diffraction orders would require modification of eq 8. The only necessary condition is that the coupling matrix elements satisfy the condition that  $\kappa_{mn} = \kappa_{nm}^*$ . For the modulation above, we expect  $\kappa_{mn}$  to be proportional to the overlap integral given by<sup>29</sup>

$$\kappa_{mn} = \propto \int \Delta \epsilon E_m^* E_n dx dy = \int j \frac{\Delta \sigma}{\omega} E_m^* E_n dx dy \quad (16)$$

where  $\Delta\sigma = M\sigma_0$  and  $E_m$  and  $E_n$  are the modal profiles of mode  $m$  and mode  $n$ , respectively. Our system has  $\omega\tau \gg 1$ , which implies  $\text{Re}(\sigma_0) \ll \text{Im}(\sigma_0)$  and  $\text{Im}(\Delta\epsilon) \approx 0$ . Ignoring dispersion ( $\Omega \ll \omega$ ), it follows that  $\kappa_{mn} \approx \kappa_{nm}^*$ .

We have directly verified eq 15 for our graphene system. We numerically calculated the absorptivity and emissivity of port 1 ( $\omega_0, g_{0x}$ ) and port 3 ( $\omega_0, -g_{0x}$ ) for our system (design A) with  $M = 0$  (unmodulated system), and  $M = 0.2$ , using the same method as Figure 2. We also performed CMT calculations assuming that the only modes that can couple are mode 1 ( $\omega_0, g_{0x}$ ) and mode 2 ( $\omega_0 + \Omega, g_{0x} - G$ ). Using the absorptivity of the unmodulated system, we directly extracted values of  $\gamma^{\text{loss}}$  and  $\gamma^{\text{rad30}}$  for port 1 and port 3. Figure 7 shows a comparison of absorptivity and emissivity calculated numerically and using CMT.

The unmodulated system in Figure 7a is reciprocal and obeys Kirchhoff's law of thermal radiation;  $\alpha(\theta) = e(\theta)$ . From eq 15,  $\alpha(\theta) = e(-\theta)$ . As a result, all four graphs in Figure 7a are identical. A good match is observed between the numerical and CMT calculations. For the modulated system, we assume that  $\gamma^{\text{loss}}$  and  $\gamma^{\text{rad}}$  are unaffected by modulation, and the only parameter that is adjusted with  $M$  is the coupling constant  $\kappa_{12}$ .  $\kappa_{12}$  was varied to fit the numerical results with CMT predictions. Figure 7b shows the numerical results for a strongly modulated system with  $M = 0.2$  compared to CMT. From the figure, we observe that  $\alpha(-36.73^\circ) = e(+36.73^\circ)$  and  $\alpha(+36.73^\circ) = e(-36.73^\circ)$ . Both CMT and numerical simulation predict nonreciprocal Rabi splitting for the absorptivity spectrum of port 1 and emissivity spectral at port 3, corresponding to the leftmost and right-most graphs in Figure 7b. These results directly verify the relationship of eq 15, which states that the absorptivity at a given input angle is equal to the emissivity at its mirror angle.

A more general proof of eq 15 comes from the compound symmetry<sup>31</sup> of the system. The system considered here is invariant under the combination of the mirror ( $x \rightarrow -x$ ) and the time-reversal ( $t \rightarrow -t$ ) operations. The time-reverse system is defined by modulation  $\tilde{\sigma} = \sigma_0 + M\sigma_0 \cos(\Omega t - Kx)$ . It can be shown that the  $S$ -matrix of the new system  $\tilde{S}$  is related by  $\tilde{S} = S^T$ .<sup>32</sup> Applying the mirror operation to the original system, we can obtain  $|S_{ab}| = |\tilde{S}_{a'b'}|$ ,<sup>33</sup> where  $a$  and  $a'$  ( $b$  and  $b'$ ) label two ports that are mirror partners. Therefore, it follows that for the original system  $|S_{ba}| = |S_{a'b'}|$ , leading to eq 15.

Thus, we can simplify the calculation process for emissivity. In the numerical computation of absorptivity above (forward problem of Figure 2a), one simulation is required. The incident frequency and wave vector are taken to correspond to  $s_{1+}$ , and the simulation output yields the  $S$ -matrix elements  $|S_{q1}|^2$ . To calculate the emissivity (inverse problem of Figure 2e), one must identify all possible input ports that generate the output  $s_{1-}$ . For each possible input port, a simulation is run to determine the value of  $|S_{1q}|^2$ . Our findings eliminate the need to solve the inverse problem.

To motivate future experimental efforts, we discuss several practical aspects of our design. A key criterion for the functioning of the proposed device is modulation speed. Graphene enables small footprint, energy efficient modulation. The modulation speed of such a device can be estimated by the time constant of the equivalent resistance–capacitance circuit.<sup>34,35</sup> Graphene-based photonic modulators have been demonstrated to operate at frequencies in the range of 150 GHz.<sup>34</sup> For the design considered in Figure 1a, assuming a footprint of  $500 \mu\text{m}^2$ , we estimate that the system capacitance is  $\sim 46$  fF. As the quantum capacitance of graphene is much higher,<sup>36</sup> the effective capacitance is determined by the

dielectric. Using a conservative value of contact resistance (50  $\Omega$ ), we estimate the cutoff frequency of modulation to be  $1/2\pi RC \sim 68$  GHz.

As the linewidths of the resonances need to be smaller than the modulation frequency, high-Q modes are critical for attaining nonreciprocity. The present design has a linewidth of approximately 2 GHz, assuming a PEC back reflector. A realistic design providing high Q could use a Bragg mirror replacing the PEC. Alternatively, the device could be modified to include an air gap between the dielectric and a gold back reflector. In our calculation, we assumed high-quality graphene with carrier mobility of  $10,000 \text{ cm}^2/\text{V s}$ .<sup>37</sup> Graphene micro-ribbons have been fabricated with carrier mobility as high as  $3000 \text{ cm}^2/\text{V s}$ .<sup>38</sup> We have verified that we can design resonances with linewidths smaller than the modulation frequency for mobility values as low as  $500 \text{ cm}^2/\text{V s}$ .

## CONCLUSIONS

In conclusion, we theoretically demonstrated the feasibility of using spatiotemporal modulation of graphene to create nonreciprocal thermal emission. Our device design creates high-quality resonances by localizing the field in a dielectric slab layer. We modulate the Fermi energy of a graphene grating on the surface of the slab in both space and time. We show that the modulation couples the guided modes of the device asymmetrically, giving rise to nonreciprocal scattering and violation of Kirchhoff's law of thermal radiation. Due to the versatility of graphene in the infrared, the structure can be designed to possess nonreciprocal emission at various wavelengths and angles of incidence. In a strongly modulated system, the spectrum displays absorptivity and emissivity "holes" that are asymmetric. The separation between the holes can be adjusted, and the holes can be moved around by changing the modulation frequency for the same system. We observe a residual symmetry between absorptivity and emissivity given by equation  $\alpha(\omega, k_x) = e(\omega, -k_x)$ . We validate our findings by comparing CMT results with numerical simulations. This relation follows from general compound symmetry considerations in adjoint systems. With this relation, exciting new properties of space–time-modulated systems emerge. These results open intriguing new possibilities for electrical control over absorptive and emissive characteristics in the infrared.

## AUTHOR INFORMATION

### Corresponding Author

Alok Ghanekar – Ming Hsieh Department of Electrical and Computer Engineering, University of Southern California, Los Angeles 90089 California, United States; [orcid.org/0000-0002-8181-481X](https://orcid.org/0000-0002-8181-481X); Email: [aghaneka@usc.edu](mailto:aghaneka@usc.edu)

### Authors

Jiahui Wang – Department of Applied Physics, Stanford University, Stanford, California 94305, United States; [orcid.org/0000-0002-0352-8287](https://orcid.org/0000-0002-0352-8287)

Cheng Guo – Department of Applied Physics, Stanford University, Stanford, California 94305, United States; [orcid.org/0000-0003-4913-8150](https://orcid.org/0000-0003-4913-8150)

Shanhui Fan – Department of Electrical Engineering, Stanford University, Stanford, California 94305, United States; [orcid.org/0000-0002-0081-9732](https://orcid.org/0000-0002-0081-9732)

Michelle L. Povinelli – Ming Hsieh Department of Electrical and Computer Engineering, University of Southern California, Los Angeles 90089 California, United States



Complete contact information is available at:  
<https://pubs.acs.org/10.1021/acsphotonics.2c01411>

## Funding

This work was funded by the Defense Advanced Research Projects Agency (DARPA) Grant HR00111820046.

## Notes

The authors declare no competing financial interest.

## REFERENCES

- (1) Li, W.; Fan, S. Nanophotonic control of thermal radiation for energy applications. *Opt. Express* **2018**, *26*, 15995–16021.
- (2) Howell, J. R.; Mengüç, M. P.; Daun, K.; Siegel, R. *Thermal Radiation Heat Transfer*; CRC press, 2020.
- (3) Modest, M. F. *Radiative Heat Transfer*; Academic press, 2013.
- (4) Lee, B. J.; Fu, C.; Zhang, Z. Coherent thermal emission from one-dimensional photonic crystals. *Appl. Phys. Lett.* **2005**, *87*, No. 071904.
- (5) Liu, X.; Tyler, T.; Starr, T.; Starr, A. F.; Jokerst, N. M.; Padilla, W. J. Taming the blackbody with infrared metamaterials as selective thermal emitters. *Phys. Rev. Lett.* **2011**, *107*, No. 045901.
- (6) Greffet, J.-J.; Carminati, R.; Joulain, K.; Mulet, J.-P.; Mainguy, S.; Chen, Y. Coherent emission of light by thermal sources. *Nature* **2002**, *416*, 61–64.
- (7) Laroche, M.; Arnold, C.; Marquier, F.; Carminati, R.; Greffet, J.-J.; Collin, S.; Bardou, N.; Pelouard, J.-L. Highly directional radiation generated by a tungsten thermal source. *Opt. Lett.* **2005**, *30*, 2623–2625.
- (8) Brar, V. W.; Sherrott, M. C.; Jang, M. S.; Kim, S.; Kim, L.; Choi, M.; Sweatlock, L. A.; Atwater, H. A. Electronic modulation of infrared radiation in graphene plasmonic resonators. *Nat. Commun.* **2015**, *6*, No. 7032.
- (9) Liu, X.; Padilla, W. J. Dynamic manipulation of infrared radiation with MEMS metamaterials. *Adv. Opt. Mater.* **2013**, *1*, 559–562.
- (10) Ries, H. Complete and reversible absorption of radiation. *Appl. Phys. B* **1983**, *32*, 153–156.
- (11) Park, Y.; Zhao, B.; Fan, S. Reaching the ultimate efficiency of solar energy harvesting with a nonreciprocal multijunction solar cell. *Nano Lett.* **2022**, *22*, 448–452.
- (12) Zhu, L.; Fan, S. Near-complete violation of detailed balance in thermal radiation. *Phys. Rev. B: Condens. Matter Mater. Phys.* **2014**, *90*, No. 220301.
- (13) Zhao, B.; Shi, Y.; Wang, J.; Zhao, Z.; Zhao, N.; Fan, S. Near-complete violation of Kirchhoff's law of thermal radiation with a 0.3 T magnetic field. *Opt. Lett.* **2019**, *44*, 4203–4206.
- (14) Shayegan, K. J.; Zhao, B.; Kim, Y.; Fan, S.; Atwater, H. A. Nonreciprocal infrared absorption via resonant magneto-optical coupling to InAs. *Sci. Adv.* **2022**, *8*, No. eabm4308.
- (15) Ghanekar, A.; Wang, J.; Fan, S.; Povinelli, M. L. Violation of Kirchhoff's Law of Thermal Radiation with Space–Time Modulated Grating. *ACS Photonics* **2022**, *9*, 1157–1164.
- (16) Meng, H.; Jang, L.; Liu, G.; Xue, X.; Lin, Q.; Zhai, X. Tunable graphene-based plasmonic multispectral and narrowband perfect metamaterial absorbers at the mid-infrared region. *Appl. Opt.* **2017**, *56*, 6022–6027.
- (17) Gao, W.; Shu, J.; Qiu, C.; Xu, Q. Excitation of plasmonic waves in graphene by guided-mode resonances. *ACS Nano* **2012**, *6*, 7806–7813.
- (18) Li, W.; Chen, B.; Meng, C.; Fang, W.; Xiao, Y.; Li, X.; Hu, Z.; Xu, Y.; Tong, L.; Wang, H.; et al. Ultrafast all-optical graphene modulator. *Nano Lett.* **2014**, *14*, 955–959.
- (19) Yu, Z.; Fan, S. Complete optical isolation created by indirect interband photonic transitions. *Nat. Photonics* **2009**, *3*, 91–94.
- (20) Bloembergen, N. Conservation laws in nonlinear optics. *J. Opt. Soc. Am.* **1980**, *70*, 1429–1436.
- (21) Miller, D. A. B.; Zhu, L.; Fan, S. Universal modal radiation laws for all thermal emitters. *Proc. Natl. Acad. Sci. U.S.A.* **2017**, *114*, 4336–4341.
- (22) Jiang, X.; Liu, W.; Zhang, B.; Sun, X. Tunable Ultra-High Q-Factor and Figure of Merit based on Fano Resonance in Graphene–Dielectric Multilayer Corrugated Structure. *Adv. Opt. Mater.* **2020**, *8*, No. 2001443.
- (23) Shi, Y.; Han, S.; Fan, S. Optical circulation and isolation based on indirect photonic transitions of guided resonance modes. *ACS Photonics* **2017**, *4*, 1639–1645.
- (24) Shi, Y.; Shin, W.; Fan, S. Multi-frequency finite-difference frequency-domain algorithm for active nanophotonic device simulations. *Optica* **2016**, *3*, 1256–1259.
- (25) García de Abajo, F. J. Graphene plasmonics: challenges and opportunities. *ACS Photonics* **2014**, *1*, 135–152.
- (26) Lin, Q.; Wang, J.; Fan, S. Compact dynamic optical isolator based on tandem phase modulators. *Opt. Lett.* **2019**, *44*, 2240–2243.
- (27) Guo, Y.; Fan, S. Narrowband thermal emission from a uniform tungsten surface critically coupled with a photonic crystal guided resonance. *Opt. Express* **2016**, *24*, 29896–29907.
- (28) Suh, W.; Wang, Z.; Fan, S. Temporal coupled-mode theory and the presence of non-orthogonal modes in lossless multimode cavities. *IEEE J. Quantum Electron.* **2004**, *40*, 1511–1518.
- (29) Fang, K.; Yu, Z.; Fan, S. Photonic Aharonov-Bohm effect based on dynamic modulation. *Phys. Rev. Lett.* **2012**, *108*, No. 153901.
- (30) Audhkhasi, R.; Povinelli, M. L. Generalized multi-channel scheme for secure image encryption. *Sci. Rep.* **2021**, *11*, No. 22669.
- (31) Guo, C.; Zhao, B.; Fan, S. Adjoint Kirchhoff's Law and General Symmetry Implications for All Thermal Emitters. *Phys. Rev. X* **2022**, *12*, No. 021023.
- (32) Asadchy, V. S.; Mirmoosa, M. S.; Diaz-Rubio, A.; Fan, S.; Tretyakov, S. A. Tutorial on electromagnetic nonreciprocity and its origins. *Proc. IEEE* **2020**, *108*, 1684–1727.
- (33) Zhao, B.; Wang, J.; Zhao, Z.; Guo, C.; Yu, Z.; Fan, S. Nonreciprocal Thermal Emitters Using Metasurfaces with Multiple Diffraction Channels. *Phys. Rev. Appl.* **2021**, *16*, No. 064001.
- (34) Phare, C. T.; Daniel Lee, Y.-H.; Cardenas, J.; Lipson, M. Graphene electro-optic modulator with 30 GHz bandwidth. *Nat. Photonics* **2015**, *9*, 511–514.
- (35) Liu, J.; Khan, Z. U.; Wang, C.; Zhang, H.; Sarjoghian, S. Review of graphene modulators from the low to the high figure of merits. *J. Phys. D: Appl. Phys.* **2020**, *53*, No. 233002.
- (36) Xia, J.; Chen, F.; Li, J.; Tao, N. Measurement of the quantum capacitance of graphene. *Nat. Nanotechnol.* **2009**, *4*, 505–509.
- (37) Banszerus, L.; Schmitz, M.; Engels, S.; Dauber, J.; Oellers, M.; Haupt, F.; Watanabe, K.; Taniguchi, T.; Beschoten, B.; Stampfer, C. Ultrahigh-mobility graphene devices from chemical vapor deposition on reusable copper. *Sci. Adv.* **2015**, *1*, No. e1500222.
- (38) Bang, K.; Chee, S.-S.; Kim, K.; Son, M.; Jang, H.; Lee, B. H.; Baik, K. H.; Myoung, J.-M.; Ham, M.-H. Effect of ribbon width on electrical transport properties of graphene nanoribbons. *Nano Convergence* **2018**, *5*, No. 7.